



Yield strength modeling of an Al-Cu-Li alloy through circle rolling and flow stress superposition approach



Purnima Bharti ^a, Ripudaman Singh ^a, Jyoti Ranjan Sahoo ^a, Aparna Tripathi ^b, Sumeet Mishra ^{a,*}

^a Department of Metallurgical and Materials Engineering, Indian Institute of Technology Roorkee, Roorkee 247667, India

^b Department of Fuel, Minerals and Metallurgical Engineering, Indian Institute of Technology Dhanbad, Dhanbad 826004, India

ARTICLE INFO

Keywords:
Al-Cu-Li alloy
Plastic deformation
Dislocations
Precipitates
Yield strength
Simulations

ABSTRACT

In the present work, the shear stress required to move a dislocation through an array of randomly distributed T_1 precipitates (Al_2CuLi), forest dislocations and solutes was computed using the circle rolling method. The evolution of shear stress as a function of swept area was determined to calculate the shear resistance of T_1 precipitates, forest dislocations and solutes for different ageing conditions. The inputs for the circle rolling simulations, such as the critical breaking angle of the obstacles, were obtained by performing detailed microstructural analysis at different length scales to estimate forest dislocation density, diameter, thickness, and number density of T_1 precipitates. The individual shear resistance of precipitates, dislocations and solutes were suitably superimposed using a flow stress addition law, where the superposition exponent is dependent on the critical breaking angles of the T_1 precipitates, forest dislocations and solutes. The present approach outperforms previous models based on the linear superposition of strengthening components in predicting the yield strength evolution of AA 2195 alloy as a function of pre-strain.

1. Introduction

Al-Cu-Li alloys have been successfully used to replace the conventional AA 2219 alloy (Al-6 wt%Cu) for space related applications such as cryogenic fuel tanks due to higher modulus and strength and lower density [1,2]. The higher strength arises from the fine dispersion of plate-shaped semi-coherent T_1 precipitates on the $\{111\}_{Al}$ plane [3,4]. During the initial stages of research on Al-Cu-Li alloys, T_1 precipitates were considered to be non-shearable in nature [5]. A modified version of Orowan equation for precipitates lying on $\{111\}_{Al}$ planes was developed to calculate the strengthening contribution from T_1 precipitates [6]. However, using high resolution transmission electron microscope, Deschamps and co-workers [7] have demonstrated that T_1 precipitates were sheared by mobile dislocations on the active slip plane. Moreover, the shearing propensity of the T_1 precipitates was observed to be vastly different from other shearable precipitates such as β'' and η' observed in the AA 6xxx and AA 7xxx series Al alloys, respectively. In contrast to repeated shearing of β'' and η' precipitates by an avalanche of dislocations [8], T_1 precipitates undergo a single shearing event on a given plane [7]. Deschamps and co-workers attributed the unconventional behavior of T_1 precipitates to creation of a high energy

matrix-precipitate interface [7]. In addition, the creation of a stacking fault was also observed owing to shearing of the T_1 precipitates [6,7]. Based on these TEM observations, Dorin et al. [6] modified the interfacial strengthening model developed by Nie and Muddle [9] to account for stacking faults. The unconventional dislocation- T_1 precipitate interaction results in a relatively homogenous plastic deformation characterized by finely spaced slip lines of smaller heights [7]. In terms of work hardening, the Kocks-Mecking plot revealed a significantly higher work hardening rate in the presence of T_1 precipitates compared to other shearable precipitates (η' in AA 7xxx) observed in Al alloys [7]. Therefore, outstanding mechanical performance can be achieved in Al-Cu-Li alloys owing to the presence of the T_1 precipitates.

To ensure the formation of T_1 precipitates in the microstructure, it is necessary to apply some degree of plastic deformation before the final ageing treatment [6,7,10,11]. The plastic deformation is usually applied via a pre-stretching operation to develop a spatially homogenous distribution of dislocations in the Al matrix, which act as nucleation sites for T_1 precipitates. Rodgers and Prangnell [10] analyzed the evolution of the average dislocation density and dislocation patterning during pre-stretching and subsequent artificial ageing. An insignificant change in the average dislocation density was observed even after a long

* Corresponding author.

E-mail addresses: sumeet.mishra@mt.iitr.ac.in, sumeet.igit@gmail.com (S. Mishra).

duration artificial ageing treatment, indicating sluggish recovery kinetics. The low level of recovery has important implications for the final T8 temper (pre-strained + artificially aged) strength, as the dislocation density introduced during the cold working operation will substantially contribute to the final strength apart from the precipitate-induced strengthening. The sluggish recovery kinetics can be attributed to several factors, such as the high Cu content (~4 wt%) in Al-Cu-Li alloys and segregation of Cu and Mg solutes towards dislocations [10,12–14].

Considering the dominant role of dislocations on the final T8 strength, Rodgers and Prangnell [10] attempted to delineate the strengthening contribution from forest dislocations and T_1 precipitates by using a linear superposition-based yield strength model. However, there have been several studies in the past, where it has been shown that linear superposition of strengthening terms is not appropriate, especially when obstacle strength and number densities are comparable [15,16]. Moreover, the individual strengthening contributions from the forest dislocations and T_1 precipitates were computed disregarding the statistical distribution of obstacles on the slip plane. Based on the classical works of Foreman and Makin [17], Nogaret and Rodney [18] and Kocks [19], it is essential to consider the statistical distribution of obstacles on the glide plane for realistic strength calculations. In the present study, we have employed the circle rolling procedure first introduced by Foreman and Makin [17] to calculate the shear resistance of forest dislocations, T_1 precipitates and solutes. Subsequently, the superposition exponents ' q ' and ' n ' were determined using the critical breaking angles of the forest dislocations, T_1 precipitates and solutes for the accurate superposition of the strengthening contributions and predict the yield strength evolution of AA 2195 alloy as a function of pre-strain. We have employed different levels of pre-strain varying from 5% to 20% to cover a range of dislocation densities and T_1 precipitate parameters (diameter and number density) and illustrate the dependence of the superposition exponents ' q ' and ' n ' on microstructural features. The modeling work is supplemented by detailed microstructural characterization via TEM, X-ray diffraction line profile analysis, and electron back scatter diffraction.

2. Experimental details

AA 2195 sheets of 1 mm thickness and composition (wt%) Al-3.7Cu-0.8Li-0.25Mg-0.08Zr-0.1Mn-0.25Ag were received from Constellium, France. Tensile specimens (Fig. 1a) with a gauge length 25 mm and gauge width 6 mm were machined from the as-received sheets. The tensile samples were annealed at 510 °C (temperature determined using thermodynamic database TCAL7 in Thermo-Calc) for 1 h, followed by rapid cooling in ice-cooled water to achieve the solutionized condition. The solutionized samples were pre-strained (along the rolling direction) at room temperature to plastic strain values ranging from 5% to 20%. The pre-strained samples were subjected to artificial ageing at 150 °C for 32 h to achieve the peak aged condition. The processing cycle is schematically shown in Fig. 1b.

Hardness and uniaxial tensile tests were performed to determine the mechanical properties of the pre-strained samples. Hardness measurements were performed using a Struers Duramin-40 hardness tester with a load of 500 kgf and dwell time of 10 s. A minimum of ten readings were obtained for each sample to ensure repeatability. Tensile tests were performed using an Instron 5982 universal testing machine with a 100 kN load cell. The tests were performed in conjunction with an axial clip-on extensometer. At least three tensile tests were performed for each condition to ensure statistical reliability.

The crystallographic texture of the solutionized sample was determined by measuring four incomplete pole figures, (111), (200), (220) and (311), at the mid-thickness of the sample. The incomplete pole figures were used to obtain the orientation distribution function (ODF) using MTEX 5.8 software [20]. The microstructures of the pre-strained samples were analyzed using electron back scatter diffraction (EBSD). A Carls Zeiss Evo 18 scanning electron microscope (SEM) equipped with a Nordlys detector (from Oxford instruments) was used for EBSD. Post-processing of EBSD data was performed using MTEX 5.8 software. The sample preparation for EBSD involved electropolishing using a Struers A2 electrolyte comprising 78 ml perchloric acid, 90 ml butoxyethanol, 100 ml distilled water, and 732 ml ethanol. The electrolyte was kept at –10 °C during the entire process.

X-ray diffraction measurements were performed using a Rigaku SmartLab goniometer to determine the dislocation density of pre-strained samples. The acceleration voltage, current, step size and 2θ range were 40 kV, 30 mA, 0.02° and 30–120°, respectively. XRD measurements were also performed on a silicon standard sample using the same parameters as those of the actual samples to separate instrument broadening. Transmission electron microscopy (TEM) studies were performed using a 300 kV JEOL 3200FS microscope to characterize the strengthening precipitates in the artificially aged samples. Twin-jet electropolishing using a mixture of 70% methanol and 30% nitric acid was used to prepare the TEM samples. The temperature of the electrolyte was kept at –25 °C. Netzsch DSC 2014 F1 was used to perform Differential scanning calorimetry (DSC) studies to evaluate the role of pre-strain on ageing kinetics.

3. Circle rolling methodology

For circle rolling simulations, a 2D simulation box (normalized dimension: 1 × 1) representing the glide plane of the dislocation was created. The simulation box was populated with a finite number (N) of randomly distributed point obstacles (Fig. 2a). Each point obstacle was associated with a certain critical breaking angle (φ_c). The left and right-hand sides of the simulation box acted as mirror boundaries. The model uses dimensionless radius (R^*) and shear stress (τ^*) for the overall calculation.

$$\tau^* = \frac{\tau b L'}{2T}; L' = \frac{1}{\sqrt{N}} \quad (1)$$

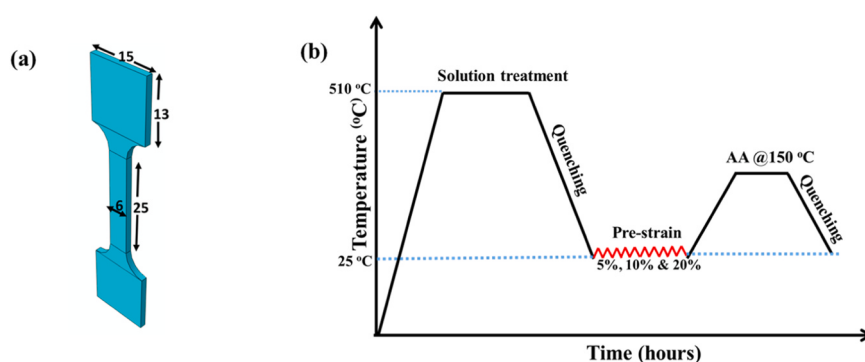


Fig. 1. (a) Schematic of the tensile specimen (all dimensions are in mm) (b) Schematic of the processing cycle used in the present work.

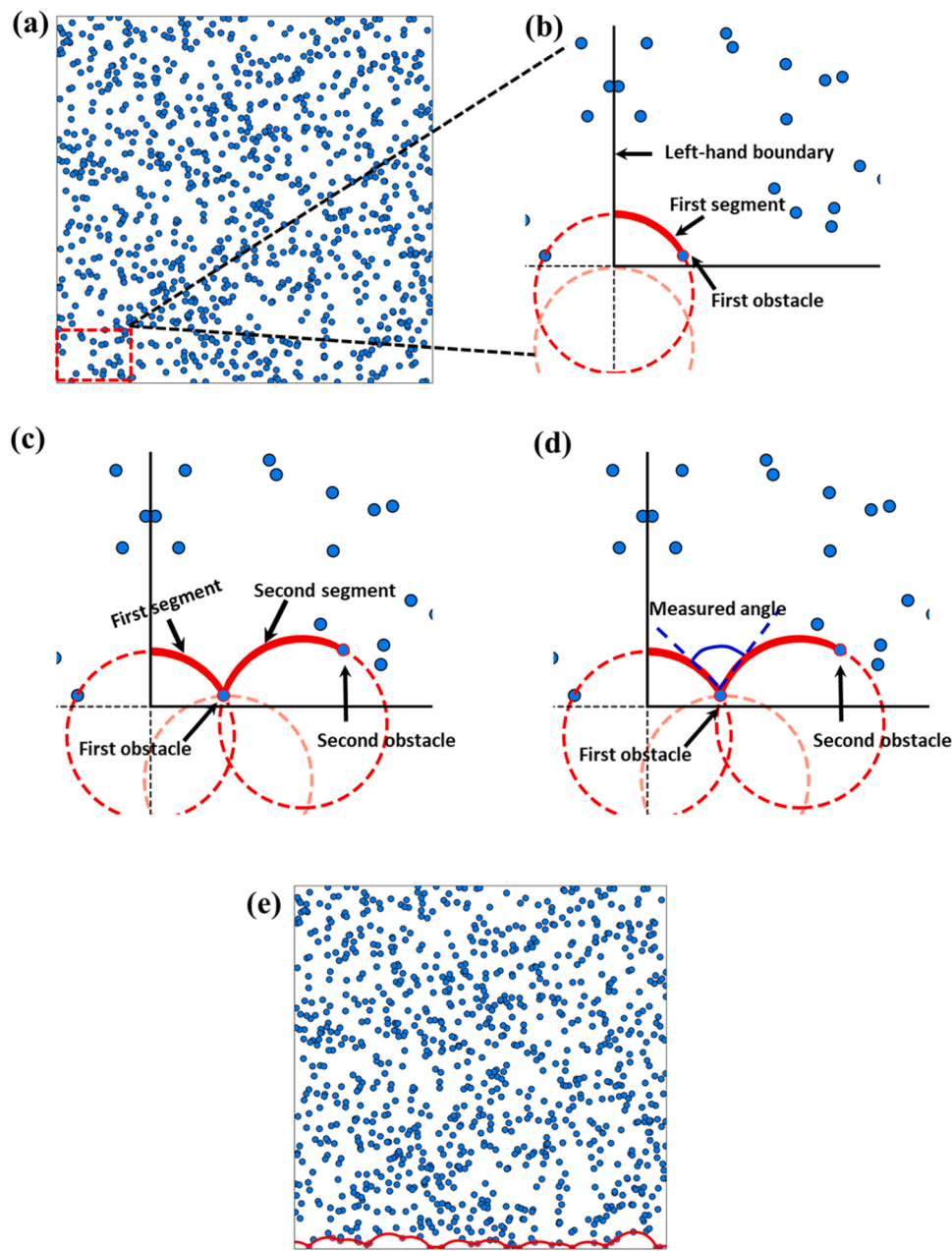


Fig. 2. (a) Simulation box populated with randomly distributed point obstacles (b) Magnified image of the left corner of the simulation box illustrating the process of finding the 1st obstacle and the 1st segment of dislocation by circle rolling (c) Magnified image of the left corner of the simulation box illustrating the process of finding the 2nd obstacle and the 2nd segment of dislocation by circle rolling (d) Measuring the angle constructed by the tangents on the two arcs of the 1st obstacle to check the validity of the 2nd obstacle (e) Stable dislocation configuration extending from the left to the right side of the simulation box for a given value of τ^* .

$$R^* = 0.5 \frac{L'}{\tau^*} \quad (2)$$

Initially, a very small value of τ^* (0.001) was selected to calculate the dimensionless radius R^* . Subsequently, a circle of radius R^* was moved up on the left-hand side of the boundary of the simulation box, until it touches an obstacle (Fig. 2b). The arc made by the left-hand side of the boundary and the obstacle is the 1st segment of the dislocation, which impinges on the boundary normally and ensures mirror boundary conditions.

The circle was then rotated counterclockwise about the 1st obstacle until it encountered the 2nd obstacle (Fig. 2c). The arc created between the 1st and 2nd obstacle is the 2nd segment of the dislocation. The angle constructed by the tangents on the two arcs of the 1st obstacle was measured (Fig. 2d). If the measured angle was greater than the critical breaking angle, the procedure of rotating the circle about the 2nd obstacle to find the 3rd obstacle was continued. However, if the measured angle at the 1st obstacle was less than the critical breaking

angle, the 2nd obstacle was ignored and the search for new obstacle was resumed by rotating the circle about the 1st obstacle.

The dislocation line was obtained by repeating the aforementioned procedure until the right-hand side of the boundary was reached (Fig. 2e). Such a dislocation line extending from the left to the right side of the simulation box was considered as the stable dislocation configuration for the chosen value of τ^* .

In the subsequent iterations, τ^* was increased in small increments and the above-mentioned procedure was repeated to determine the stable dislocation configuration at different values of τ^* . There will be a particular scenario, where, at a given value of τ^* , the dislocation line will sweep through the entire simulation box in search of a stable configuration. In such a situation, τ^* value in the previous iteration was identified as the critical resolved shear stress (τ_{crss}^*). We illustrate two examples of circle rolling simulations corresponding to strong ($\varphi_c = 40^\circ$) and weak ($\varphi_c = 160^\circ$) obstacle regimes. The last stable dislocation configuration before the dislocation sweeps across the simulation box is shown in Fig. 3(a-b). It can be observed that the dislocation line remains

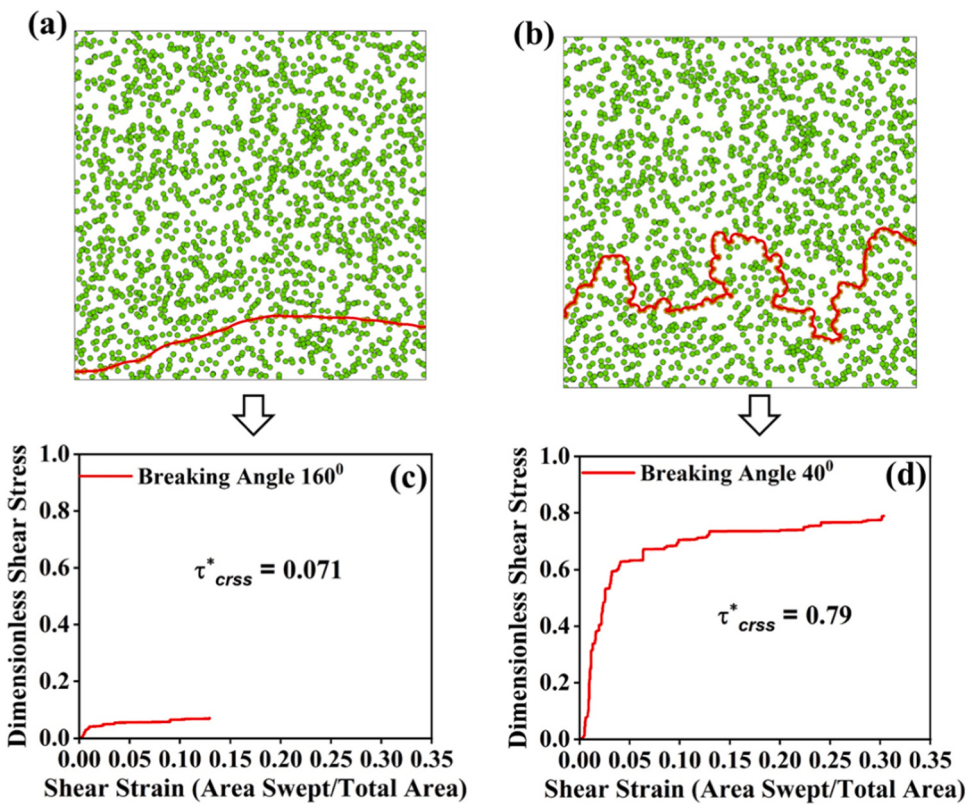


Fig. 3. (a) Last stable dislocation configuration for $\varphi_c = 160^\circ$ (b) Last stable dislocation configuration for $\varphi_c = 40^\circ$ (c) Dimensionless shear stress versus shear strain curve for $\varphi_c = 160^\circ$ (d) Dimensionless shear stress versus shear strain curve for $\varphi_c = 40^\circ$.

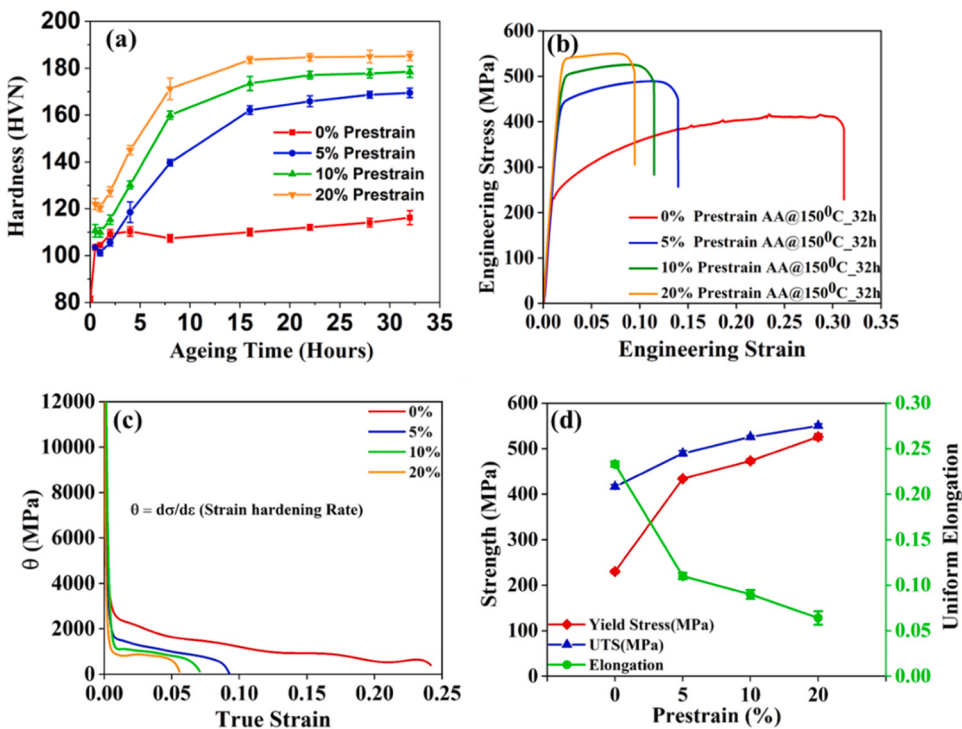


Fig. 4. (a) Evolution of hardness with ageing time (ageing temperature=150 °C) for different pre-strain amount (b) Engineering stress versus Engineering strain curves for different pre-strained samples after 32 h artificial ageing at 150 °C (c) Work hardening rate (θ) versus true strain curves for different pre-strained samples after 32 h artificial ageing at 150 °C (d) Yield strength, ultimate tensile strength and uniform elongation plotted as a function of pre-strain.

fairly straight (less curvature) during its motion through an array of weak obstacles. On the other hand, the dislocation line developed a significant curvature in the strong-obstacle regime. The corresponding shear stress versus shear strain curves are shown in Fig. 3(c-d). The maxima in these curves correspond to the dimensionless critical resolved shear stress.

4. Results

The age-hardening curves as a function of pre-strain level are shown in Fig. 4a. The curves demonstrate the positive impact of plastic deformation on the ageing behavior. A marked difference in peak hardness can be observed between the pre-strained and undeformed samples. After 32 h of ageing, the difference in hardness between the 5% pre-strained sample and the undeformed sample is close to ~55 HVN. For the pre-strained samples, the peak hardness continued to increase with increasing pre-deformation, although at a decreasing rate. The age-hardening curves reveal that the maximum increase in hardness for the pre-strained samples occurs during the initial 8–12 h of ageing, followed by a plateau region up to 32 h. Previous literature on AA 2195 also suggests a peak ageing time of ~24–32 h and a stable peak hardness close to 100 h [10].

The peak-aged samples (32 h aged) at different pre-strain levels were selected for further analysis via tensile testing. The engineering stress

versus engineering strain curves for the representative samples are shown in Fig. 4b. It can be clearly observed that the yield strength of the 5% pre-strained sample is nearly double of the undeformed sample. For the pre-strained samples, the yield strength increased by nearly ~100 MPa with an increase in pre-strain from 5% to 20%. The increase in the strength of the pre-strained samples occurred at the expense of ductility. Fig. 4c shows the work-hardening rate as a function of the true strain for the representative samples. It can be clearly observed that the undeformed sample is able to maintain a relatively higher work hardening rate compared to the pre-deformed samples at all stages of plastic deformation. Therefore, the 0% pre-strained sample exhibited the highest ductility compared to the pre-strained samples. Important results, such as the yield and ultimate tensile strength, and uniform elongation are summarized in Fig. 4d.

To estimate the effect of plastic deformation on the dislocation density, X-ray diffraction line profile analysis was performed using the convolutional multiple whole profile (CMWP) fitting software developed by Ungar and co-workers [21]. The CMWP software considers theoretical profile functions corresponding to the crystallite size ($I_{hkl}^{crystallite}$), dislocation density ($I_{hkl}^{dislocations}$), and instrument broadening ($I_{hkl}^{instrument}$). The theoretical profile ($I_{hkl}^{theoretical}$) can be written as

$$I_{hkl}^{theoretical}(\theta) = \sum_{hkl} I_{hkl}^{dislocations} \times I_{hkl}^{crystallite} \times I_{hkl}^{instrument} + I_{hkl}^{background} \quad (3)$$

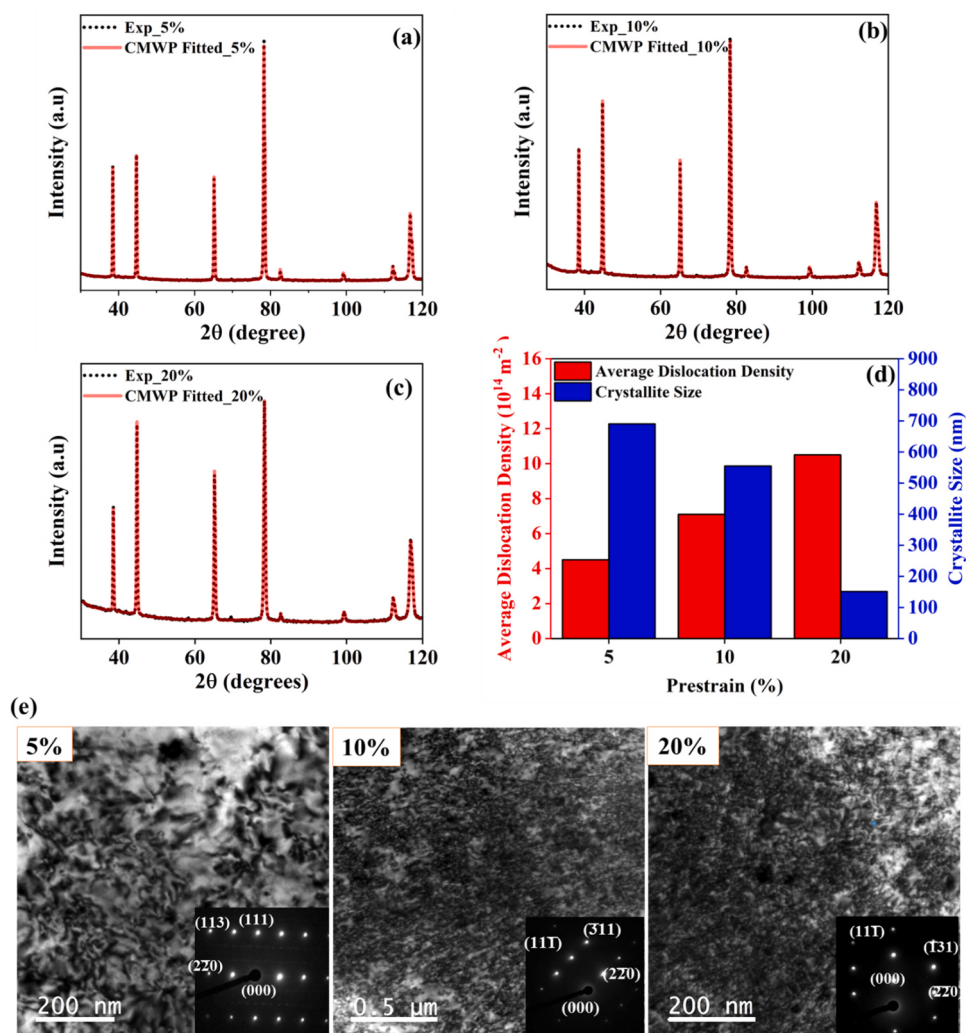


Fig. 5. (a) Experimental and Simulated XRD patterns after different pre-strain levels (a) 5% (b) 10% (c) 20% (d) Evolution of dislocation density and crystallite size after different pre-strain amount (e) TEM dislocation substructure after different pre-strain amount.

Here, $I_{hkl}^{background}$ represents the background of the experimentally determined profile, which is added to the convolution of theoretical profiles. Subsequently, the theoretical profile ($I^{theoretical}$) is matched with the experimental profile by adjusting the model parameters such as the dislocation character, crystallite size, dislocation density, and dislocation arrangement parameter. Fig. 5(a-c) represents the agreement between experimental and simulated XRD patterns. The evolution of the dislocation density and crystallite size is summarized in Fig. 5d. It can be observed that the dislocation density increases with pre-deformation and reaches around $\sim 1.0 \times 10^{15} \text{ m}^{-2}$ after 20% pre-strain. The crystallite size undergoes a marked decrease from $\sim 690 \text{ nm}$ after 5% pre-strain to $\sim 150 \text{ nm}$ after 20% pre-strain. The dislocation densities for different pre-strained samples are summarized in Table 1. It should be noted that the AA 2195 alloy exhibits sluggish recovery kinetics during low temperature artificial ageing at 150°C because of the segregation of Cu and Mg solutes towards dislocations [10]. Therefore, an insignificant change in the dislocation density is expected after artificial ageing treatment of the pre-strained samples.

TEM studies were further performed to observe the dislocation structures in the pre-deformed samples. Dense dislocation tangles and locks can be observed in the substructure with increasing amount of pre-strain (Fig. 5e). There was no evidence of dislocation cell formation even after 20% deformation. This indicates retardation of dynamic recovery due to the high solute content in the matrix. It is well established that solutes have a strong inhibiting effect on cross-slip, which is the dominant mechanism for dynamic recovery at room temperature. The dislocation arrangement in Fig. 5e resembles with commonly observed substructures in 5xxx series Al alloys, where the high solute content (Mg) plays a similar role of inhibiting cross-slip.

To observe the meso-scale effect of pre-deformation, EBSD studies were performed. Fig. 6a shows the inverse pole figure maps (IPFX || tensile axis) after different levels of pre-deformation. After 5% pre-strain, only a few grains (marked by black arrows) illustrate the presence of an orientation gradient. However, with increasing pre-deformation levels, several grains exhibited an orientation gradient, indicating heterogenous deformation. The corresponding grain orientation deviation (GROD) maps (Fig. 6b), where the pixel misorientation is evaluated with respect to the average orientation of the grain, elegantly captures the development of the orientation gradient with increasing pre-deformation level. A representative grain (Fig. 6c) is selected for each condition to demonstrate the misorientation build-up from the grain interior to the grain boundary after different levels of pre-strain. It can be observed that the 20% pre-strained sample shows a misorientation build-up of nearly 11° compared to 4° in the 5% pre-strained sample. Further indication about deformation heterogeneity can be obtained from the kernel average misorientation (KAM) maps (Fig. 6d), where the pixel misorientation is evaluated with respect to its nearest neighbors. It is well established that high KAM regions correspond to higher geometrically necessary dislocation densities [22]. The

average KAM was determined to be 0.14 and 0.51 for the 5% and 20% pre-strained samples, respectively. This suggests a higher GND density in the 20% pre-strained sample than the 5% pre-strained sample.

To understand the effect of pre-deformation on the evolution of precipitates during artificial ageing, differential scanning calorimetry studies were carried out. A representative DSC data set is provided in Fig. 7a for the samples subjected to 5% pre-strain and artificially aged at 150°C for different durations. An exothermic peak corresponding to the formation of T_1 (Al_2CuLi) precipitates can be observed at $\sim 230\text{--}250^\circ\text{C}$. It should be noted that T_1 is the main strengthening phase in the Al-Cu-Li systems. With increasing artificial ageing duration, the exothermic peak area corresponding to T_1 precipitates decreases due to the progressively higher volume fraction of T_1 precipitates being present in the matrix prior to DSC measurements. To illustrate the role of pre-strain on the T_1 precipitation kinetics, we performed DSC measurements for the 5% and 20% pre-strained samples (0-hour condition) at different heating rates ($5\text{--}20^\circ\text{C}/\text{min}$, Fig. 7b and d). The peak temperature (T_p) corresponding to the exothermic peak of the T_1 (Al_2CuLi) precipitates was identified for different heating rates (β), and the Kissinger method [23] was used to calculate the activation energy (E_a) of the formation of the T_1 precipitates.

$$\ln\left(\frac{T_p^2}{\beta}\right) = \frac{E_a}{R_g T_p} + C \quad (4)$$

Here, R_g is the gas constant and C is a constant. The plot of $\ln\left(\frac{T_p^2}{\beta}\right)$ versus $1/T_p$ (Fig. 7c and e) shows a linear relationship with a coefficient of regression of $R^2 \sim 0.99$. The activation energies deduced from the slope were 106 and 97 kJ/mol for 5% and 20% pre-strained samples, respectively. This suggests that the T_1 precipitation kinetics is enhanced by increasing the amount of pre-strain.

TEM studies were performed to quantitatively establish the diameter, thickness, number density, and distribution of the T_1 precipitates. Figs. 8–10 illustrate representative TEM images taken along the $<110>_{\text{Al}}$ and $<112>_{\text{Al}}$ zone axes for different levels of pre-strain. It can be observed that the uniformity of the distribution of T_1 precipitates increases with increasing pre-strain level. This can be attributed to the underlying dislocation substructure, where a uniform distribution of dislocations was observed at higher pre-strain levels. In addition, the average diameter of the T_1 precipitates decreases with increasing pre-strain amount (Table 1, Figs. 8c, 9c and 10c). This is due to the higher density of nucleation sites (dislocations) and consequently faster ageing kinetics with increasing pre-strain amount. The width of the T_1 precipitate diameter frequency distribution also decreases with increasing pre-strain level, which further confirms the increasing uniformity of precipitate size distribution. On the other hand, thickness of the T_1 precipitates remains more or less constant at $\sim 1.3 \text{ nm}$, irrespective of the pre-strain amount (Table 1). This indicates the formation of only single-layer T_1 precipitates in all pre-strained samples [24]. Important parameters such as the average plate diameter (D), thickness (t), and number density (N_v) are summarized in Table 1. The volume fraction of the T_1 precipitates (f_v) was calculated using the following equation [10].

$$N_v = \frac{4f_v}{\pi D t^2} \quad (5)$$

The detailed microstructural analysis presented in the above paragraphs to obtain information about the dislocation density and characteristics of T_1 precipitates will now be used in the subsequent section to predict the yield strength evolution of AA 2195 as a function of pre-strain.

4. Modeling and discussion

The yield strength of an age hardenable Al alloy with three sets of obstacles (T_1 precipitates, forest dislocations, and solutes) can be expressed as [15].

Table 1
Dislocation density, diameter, thickness, number density and volume fraction of T_1 precipitates in different pre-strained samples.

| Pre-strain (%) | Average dislocation density (in pre-strained samples) (10^{14} m^{-2}) | Diameter of T_1 precipitate (nm) | Thickness of T_1 precipitate (nm) | Number Density of T_1 precipitate (m^{-3}) | Volume Fraction of T_1 precipitates (%) |
|----------------|--|------------------------------------|-------------------------------------|--|---|
| 5 | 4.50 | 42.35 ± 15 | 1.30 ± 0.40 | 1.81E22 | 3.3 |
| 10 | 7.10 | 37.35 ± 8.8 | 1.30 ± 0.31 | 2.52E22 | 3.5 |
| 20 | 10.5 | 34.73 ± 9.8 | 1.30 ± 0.38 | 2.84E22 | 3.4 |

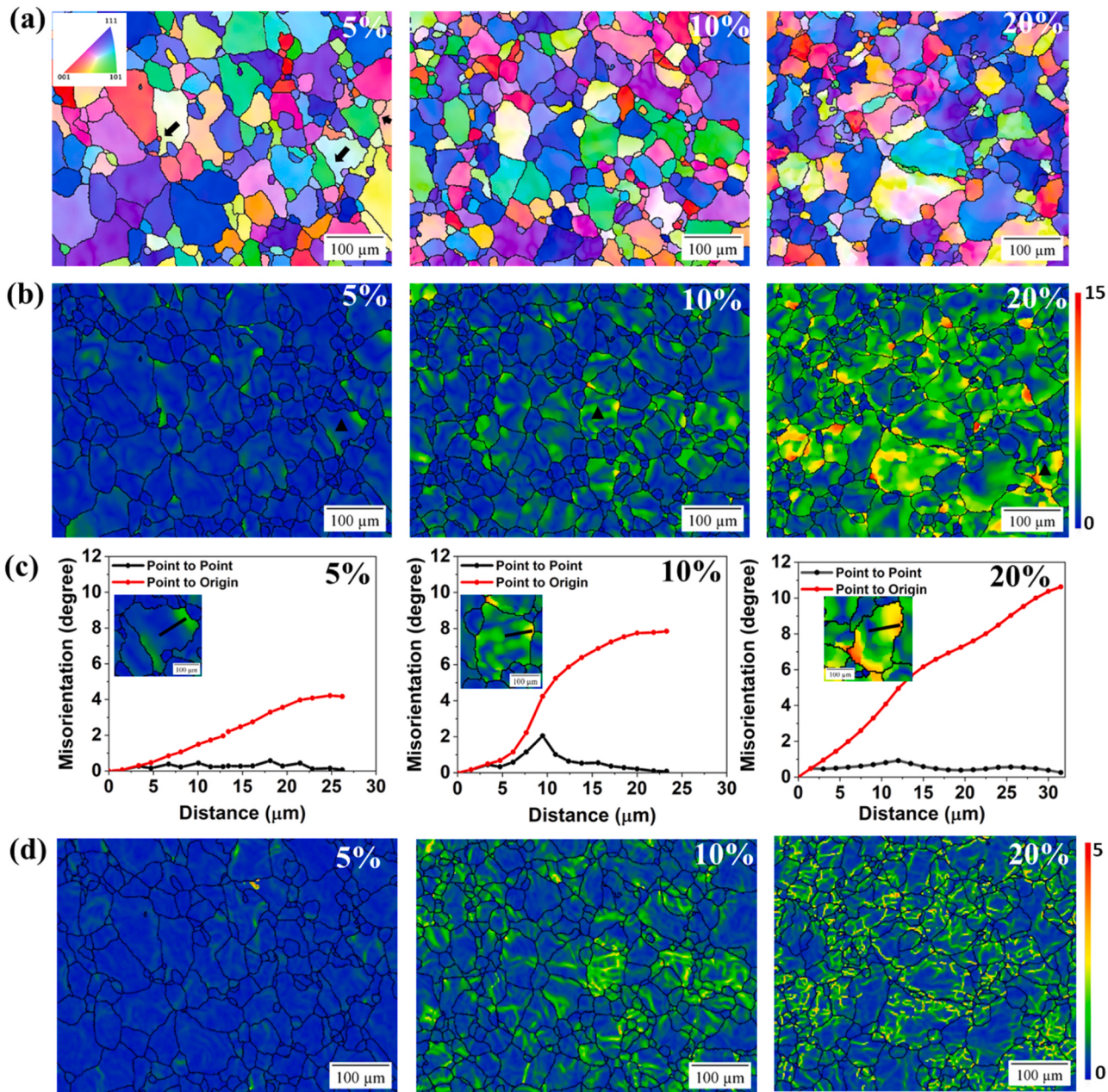


Fig. 6. (a) Inverse pole figure maps after different pre-strain levels (b) Grain reference orientation deviation (GROD) maps after different pre-strain levels (c) Point to Point and Point to Origin misorientation evolution for a representative grain after different levels of pre-strain (d) Kernel average misorientation (KAM) maps after different pre-strain levels.

$$\sigma_{yield} = \sigma_{gb} + \left[\left(\sigma_{sol}^q + \sigma_{ppt}^q \right)^{\frac{n}{q}} + \sigma_{dis}^n \right]^{\frac{1}{n}} \quad (6)$$

Here, σ_{gb} , σ_{dis} , σ_{ppt} , σ_{sol} are the strengthening contributions from the grain boundaries, forest dislocations, T_1 precipitates, and solutes, respectively. Eq. 6 reduces to the familiar linear and quadratic superposition of the flow stress if the exponents ‘ q ’ and ‘ n ’ are taken as 1 and 2, respectively. Vaucoerbeil et al. [15] examined the superposition exponents ‘ q ’ and ‘ n ’ in the framework of areal glide simulations, and suggested that the extreme values of ‘ q ’ and ‘ n ’ does not represent the wide range of obstacle strength and densities commonly observed in engineering alloys. An explicit equation based on critical breaking angle of obstacles was proposed by Vaucoerbeil et al. [15] to determine the exponents ‘ q ’ and ‘ n ’.

$$q = 1 + e^{[-\beta - (\varphi_{sol} + \varphi_{ppt})^{\delta} - (\varphi_{sol} - \varphi_{ppt})^{2m}]} \quad (7)$$

$$n = n_{ppt_dis} + (n_{sol_dis} - n_{ppt_dis}) \sqrt{1 - \left(\frac{2}{\pi} \tan^{-1} \left(\frac{N_{ppt}}{N_{sol}} \right) \right)^2} \quad (8)$$

$$n_{ppt_dis} = 1 + e^{[-\beta - (\varphi_{ppt} + \varphi_{dis})^{\delta} - (\varphi_{ppt} - \varphi_{dis})^{2m}]} \quad (9)$$

$$n_{sol_dis} = 1 + e^{[-\beta - (\varphi_{sol} + \varphi_{dis})^{\delta} - (\varphi_{sol} - \varphi_{dis})^{2m}]} \quad (10)$$

Here, φ_{sol} , φ_{ppt} and φ_{dis} are the critical breaking angles of the solutes, T_1 precipitates and forest dislocations, respectively. The parameters β , δ and m are constants with values of 0.1, 1 and 1, respectively [15]. N_{ppt} and N_{sol} represent the areal densities of precipitates and solutes, respectively. Firstly, we will demonstrate the calculation of critical

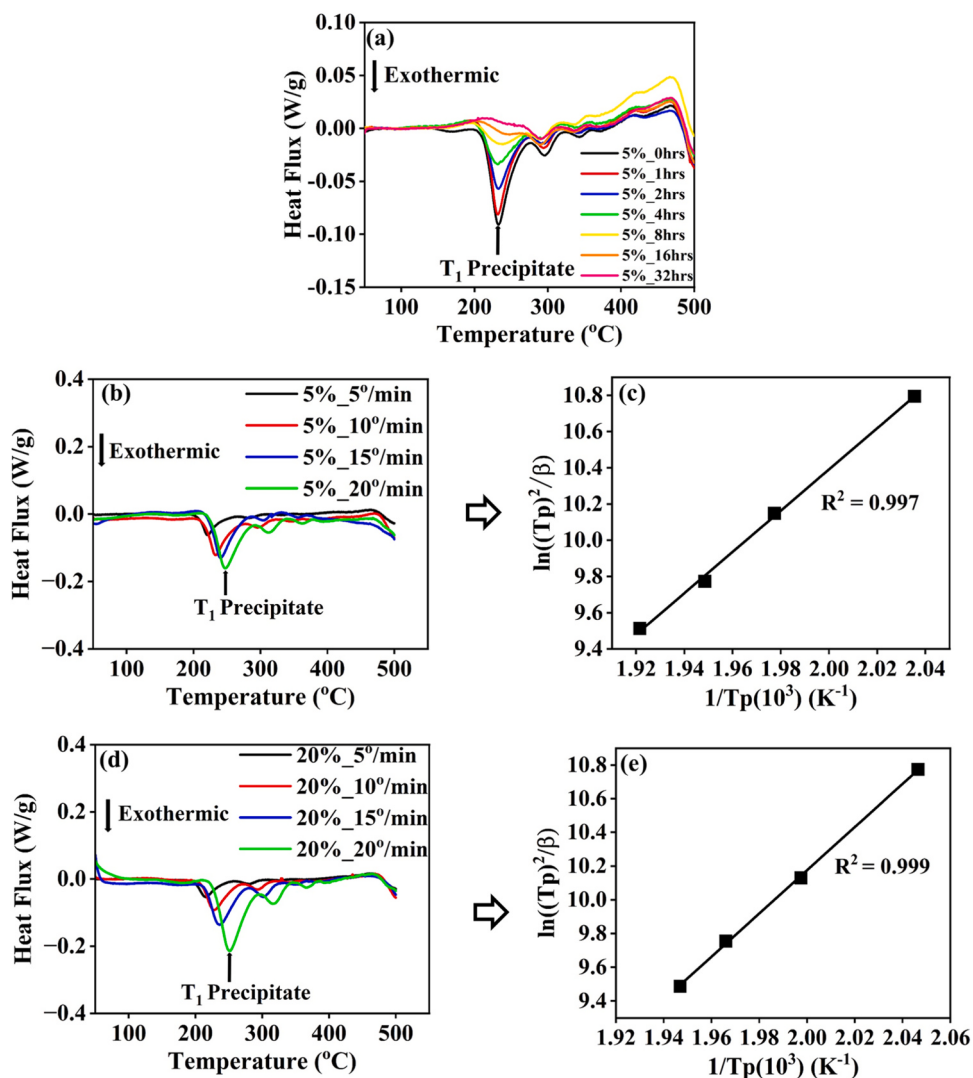


Fig. 7. (a) DSC thermograms of the 5% pre-strained sample with increasing ageing time at 150 °C (b) DSC thermograms of the 5% pre-strained sample (0 h sample) at different heating rates (c) Variation of $\ln(T_p)^2/\beta$ versus $1/T_p$ for the 5% pre-strained sample (d) DSC thermograms of the 20% pre-strained sample (0 h sample) at different heating rates (e) Variation of $\ln(T_p)^2/\beta$ versus $1/T_p$ for the 20% pre-strained sample.

breaking angles, followed by the calculation of exponents ‘q’ and ‘n’.

The critical breaking angle of the T₁ precipitates (φ_{ppt}) is related to the obstacle strength (F_{ppt}) as

$$F_{ppt} = 2T\cos\left(\frac{\varphi_{ppt}}{2}\right) \quad (11)$$

Here, T is the line tension, which can be approximated as $Gb^2/2$, where G (25,400 MPa) is the shear modulus and b (0.286 nm) is the Burgers vector. The obstacle strength can be expressed as [6].

$$F_{ppt} = \left(\frac{\pi \times \cos\omega \times \sin\theta \times b \times D}{2t} \right) \times \gamma_{eff} \quad (12)$$

$$\gamma_{eff} = \gamma_i + \left(\frac{t}{2 \times b \times \cos\omega \times \sin\theta} - \frac{1}{2} \right) \times \gamma_{SF} \quad (13)$$

Here, D is the average diameter of the T₁ precipitates, t is the thickness of the T₁ precipitates, γ_i (0.085 J m⁻²) is the interfacial energy between the T₁ precipitate and the matrix, γ_{SF} (0.005 J m⁻²) is the interfacial energy corresponding to the creation of a stacking fault, θ (70.53°) is the angle between the two {111}_{Al} planes, and ω (30°) is the angle between the Burgers vector and the <112> direction [6]. For the three representative conditions (5%, 10%, 20% pre-strained and aged at

150 °C for 32 h), obstacle strength (F_{ppt}) was calculated using Eq. 12. Subsequently, the corresponding critical breaking angle (φ_{ppt}) was determined using Eq. 11. Table 2 summarizes the values of F_{ppt} and φ_{ppt} for different conditions. It can be observed that as the T₁ precipitate diameter decreases with increasing pre-strain level, the obstacle strength (F_{ppt}) decreases, which in turn increases the critical breaking angle of T₁ precipitates. This indicates that the shear resistance of the T₁ precipitates decreased with increasing pre-strain. The critical breaking angle of the solutes (weak obstacles) was estimated to be ~178° by Vaucorbeil et al. [15]. Using φ_{ppt} and φ_{sol} , the exponent ‘q’ was calculated for different ageing condition via Eq. 7 (Table 2). The exponent ‘q’ varies between 1.56 and 1.68 for the three representative conditions. As the difference between φ_{sol} and φ_{ppt} decreases with increasing pre-strain, the exponent ‘q’ increases from 1.56 in the 5% pre-strained sample to 1.68 in the 20% pre-strained sample. These observations suggest that the previous approaches of simply assuming ‘q’ as 1 or 2 would have led to errors in strength prediction.

Following the calculation of ‘q’, we now demonstrate the calculation of the exponent ‘n’. Utilizing the critical breaking angle of forest dislocations ($\sim \varphi_{dis} = 78^\circ$) obtained by Devincre and Kubin [25] via dislocation dynamics simulations, n_{ppt_dis} and n_{sol_dis} were calculated using

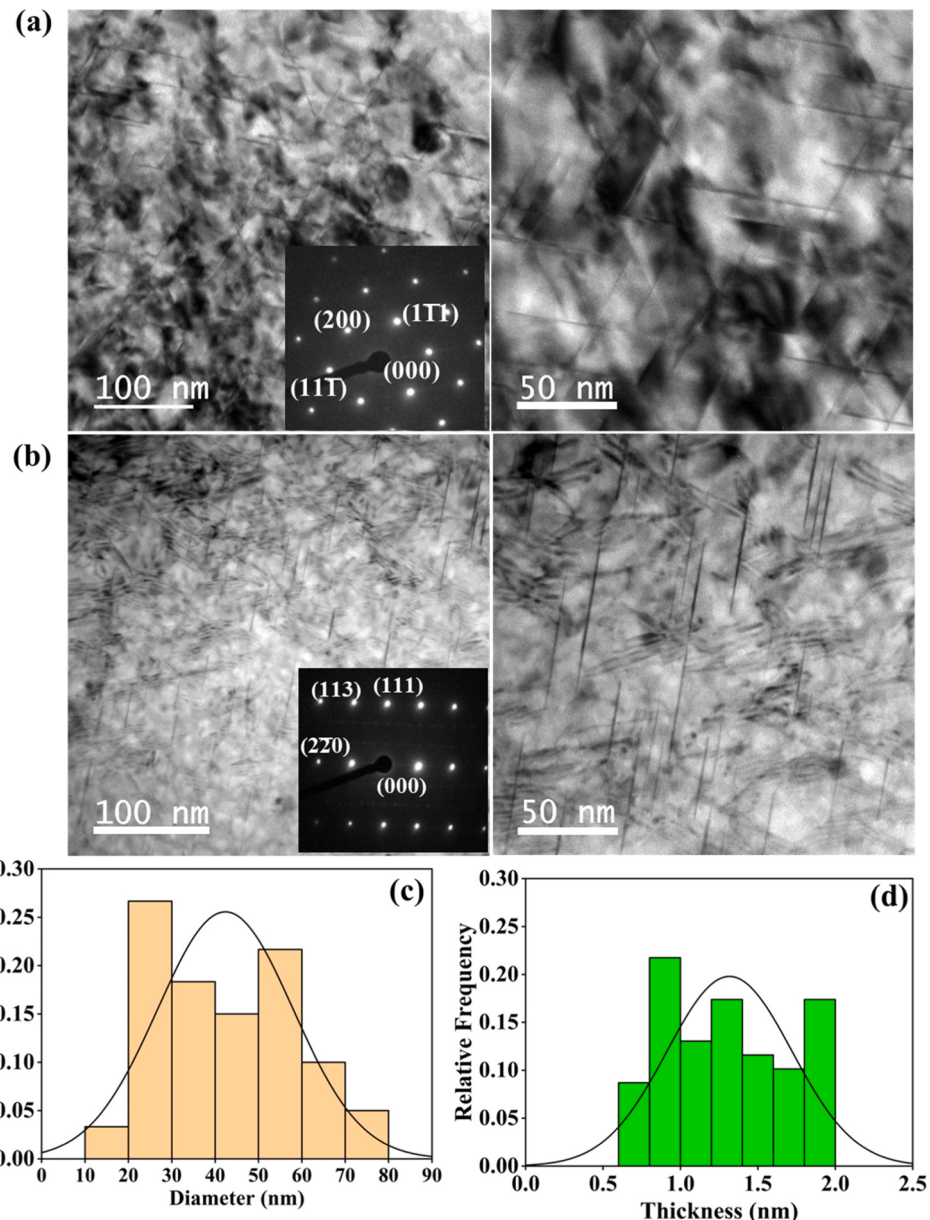


Fig. 8. TEM bright field images for the 5% pre-strained sample aged at 155 °C for thirty-two hours (a) $<110>_{\text{Al}}$ Zone axis (b) $<112>_{\text{Al}}$ Zone axis (c) Distribution of T₁ precipitate diameter (d) Distribution of T₁ precipitate thickness.

Eqs. 9 and 10. The areal densities of the precipitates and solutes (N_{ppt} and N_{sol}) were computed using the following relations [6,15].

$$L_{\text{ppt}} = 0.931 \sqrt{\frac{0.265\pi Dt}{f_v}}; N_{\text{ppt}} = \frac{1}{L_{\text{ppt}}^2} \quad (14)$$

$$L_{\text{sol}} = \frac{3^{1/4}b}{2\sqrt{c}}; N_{\text{sol}} = \frac{1}{L_{\text{sol}}^2} \quad (15)$$

Here, L_{ppt} and L_{sol} are the mean spacing of the T₁ precipitates and solutes, respectively. It has been observed via atom probe studies that some amount of solutes (Cu and Li) remain in solution even after 32 h of ageing at 155 °C [14,26]. Peters et al. [14] observed that ~0.4 at% Cu and ~3.0 at% Li remained in solution after 32 h of ageing at 155 °C for an Al-Cu-Li alloy with a similar composition to that used in the present work. Therefore, we have taken the effective solute concentration in the matrix to be 3.4 at% ($c = 0.034$) following the approach of the previous authors [14,26]. The values of $n_{\text{ppt_dis}}$, $n_{\text{sol_dis}}$, L_{ppt} , N_{ppt} , L_{sol} , N_{sol} and n are

summarized in Table 2. It can be observed that the areal density of solutes (N_{sol}) is significantly higher compared to areal density of precipitates (N_{ppt}). As a result, the square root term in Eq. 8 can be ignored. Therefore, the exponent ‘ n ’ is governed mainly by the critical breaking angles of the solutes and forest dislocations viz., $n_{\text{sol_dis}}$.

We now employ the circle rolling method to calculate the dimensionless shear resistance of the T₁ precipitates (τ_{ppt}^*), forest dislocations (τ_{dis}^*) and solutes (τ_{sol}^*), which can then be used as input in Eq. 6 to calculate yield strength. As outlined in Section 3, a simulation box with mirror boundary conditions and 10,000 obstacles was created. Each obstacle was assigned a critical breaking angle. The circle rolling simulations were performed for five cases corresponding to breaking angles of 78° (forest dislocations), 178° (solutes), 116° (T₁ precipitates in the 5% pre-strained sample), 126° (T₁ precipitates in the 10% pre-strained sample) and 130° (T₁ precipitates in the 20% pre-strained sample), respectively. It should be noted that for dilute precipitate volume fraction ($f_v \approx 0.03$) viz. $r/L_{\text{ppt}} < 1$, the T₁ precipitates can be approximated as point obstacles [27]. The outputs of the circle rolling simulations are

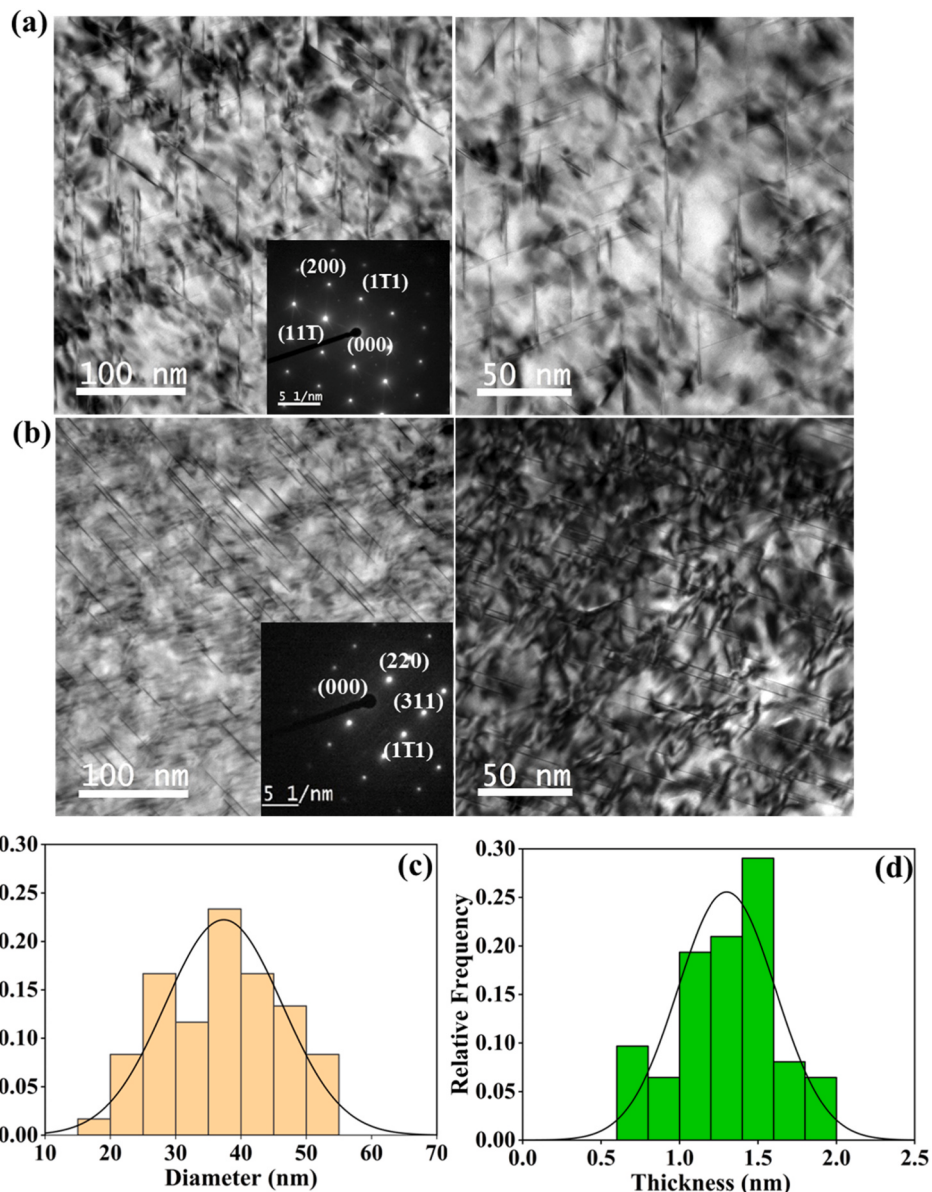


Fig. 9. TEM bright field images for the 10% pre-strained sample aged at 155 °C for thirty-two hours (a) <110>_{Al} Zone axis (b) <112>_{Al} Zone axis (c) Distribution of T₁ precipitate diameter (d) Distribution of T₁ precipitate thickness.

shown in Fig. 11 (a-e) in terms of the last stable dislocation configuration before the dislocation sweeps across the simulation box and the dimensionless shear stress versus shear strain curve. The maxima in the dimensionless shear stress versus shear strain curve corresponds to the normalized shear resistance (τ^*). It can be observed that forest dislocations exhibit the maximum shear resistance ($\tau_{dis}^* = 0.609$) due to the smaller critical breaking angle. For the T₁ precipitates, as the plate diameter decreased with increasing pre-strain, the obstacle strength decreased (critical breaking angle increased), resulting in drop in the value of τ_{ppt}^* . The solutes exhibit the minimum shear resistance ($\tau_{sol}^* = 0.002$) due to substantially higher critical breaking angle. The dimensionless shear stress values can be used in the following equations to compute σ_{dis} , σ_{ppt} and σ_{sol} .

$$\sigma_{dis} = \frac{\bar{M}Gb}{L_{dis}} \quad \tau_{dis}^*; \quad L_{dis} = \frac{1}{\sqrt{\rho}} \quad (16)$$

$$\sigma_{ppt} = \frac{\bar{M}Gb}{L_{ppt}} \tau_{ppt}^* \quad (17)$$

$$\sigma_{sol} = \frac{\bar{M}Gb}{L_{sol}} \tau_{sol}^* \quad (18)$$

Here, ρ is the average dislocation density in the different pre-strained samples (Table 1) and \bar{M} is the average Taylor factor. In order to use the above equations for calculating the strengthening contribution, the average Taylor factor (\bar{M}) needs to be determined using crystallographic texture data. Fig. 12a shows the important ODF sections of the solution-treated sample. Considering the nominal amount of plastic deformation and low temperature ageing employed in the present work, there will be no significant change in texture during pre-straining and ageing. The Taylor model is based on the concept that the external work done ($\sigma_{xx}de_{xx}$) in deforming a polycrystal is equal to the internal work ($\tau_{crss}\sum_i d\gamma_i$) by slip on all active slip systems inside a grain [28,29].

$$\sigma_{xx}de_{xx} = \tau_{crss}\sum_i d\gamma_i; M = \frac{\sum_i d\gamma_i}{de_{xx}} \quad (19)$$

Here, de_{xx} is the axial incremental strain and $d\gamma_i$ is the incremental shear on slip system ' i '. In the present work, the MTEX-5.8 software was

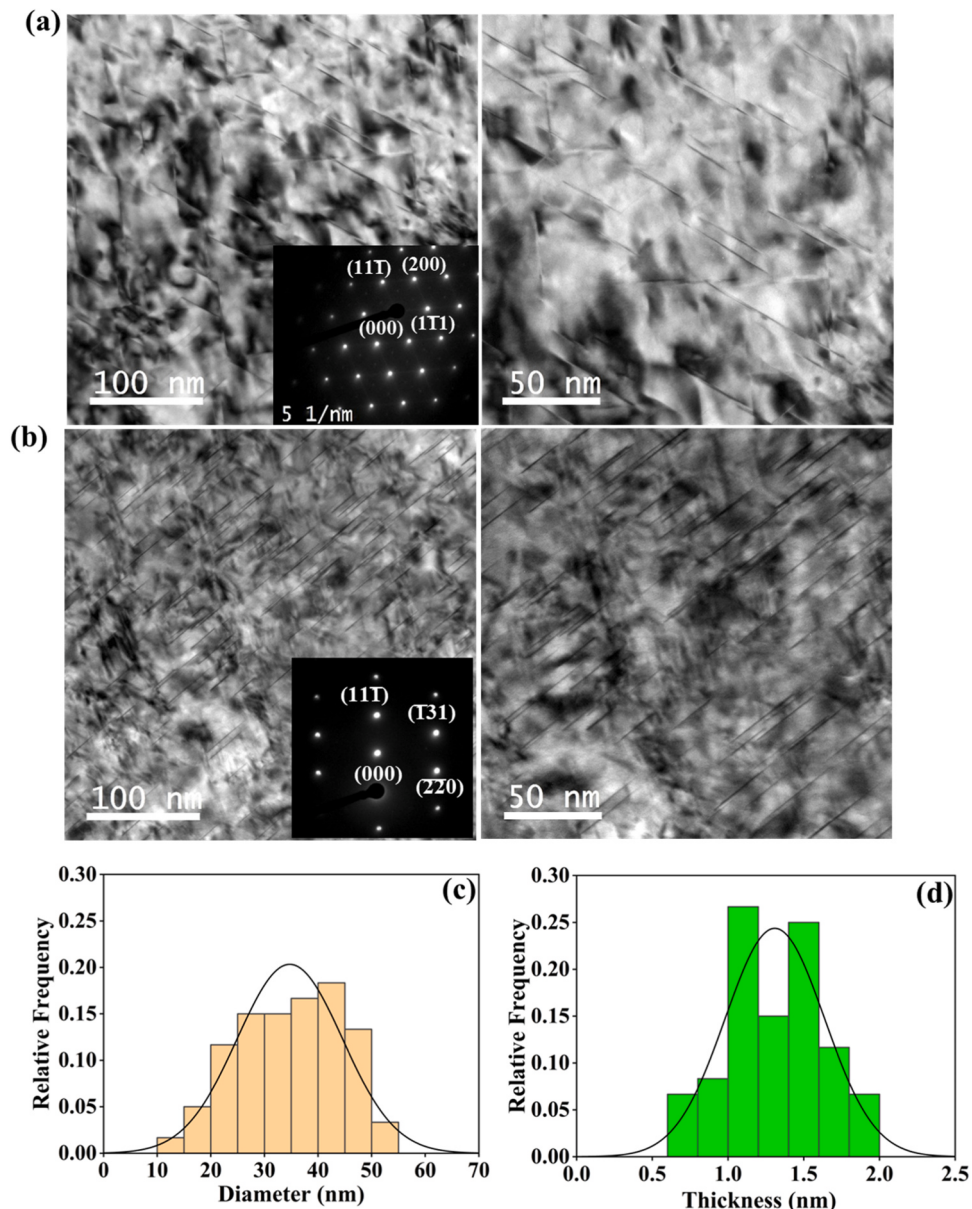


Fig. 10. TEM bright field images for the 20% pre-strained sample aged at 155 °C for thirty-two hours (a) <110>_{Al} Zone axis (b) <112>_{Al} Zone axis (c) Distribution of T₁ precipitate diameter (d) Distribution of T₁ precipitate thickness.

Table 2

Summary of T₁ precipitates obstacle strength (F_{ppt}), T₁ precipitates critical breaking angle, superposition parameters ‘q’, n_{ppt_dis} , n_{sol_dis} , n, T₁ precipitates spacing (L_{ppt}), areal density of T₁ precipitates (N_{ppt}), solute spacing (L_{sol}) and areal density of solutes (N_{sol}) for different pre-strained samples.

| Pre-strain | F_{ppt} (N) | φ_{ppt} | q | n_{ppt_dis} | n_{sol_dis} | L_{ppt} (m) | N_{ppt} (m ⁻²) | L_{sol} (m) | N_{sol} (m ⁻²) | n |
|------------|---------------|-----------------|------|----------------|----------------|---------------|------------------------------|---------------|------------------------------|------|
| 5% | 1.1E-9 | 118° | 1.56 | 1.84 | 1.25 | 3.40E-8 | 8.63E14 | 1.04E-9 | 9.25E17 | 1.25 |
| 10% | 1E-9 | 126° | 1.64 | 1.77 | 1.25 | 3.20E-8 | 9.80E14 | 1.04E-9 | 9.25E17 | 1.25 |
| 20% | 9.2E-10 | 130° | 1.68 | 1.74 | 1.25 | 3.06E-8 | 1.06E15 | 1.04E-9 | 9.25E17 | 1.25 |

used to discretize the ODF and generate 10,000 single orientations. Subsequently, ‘M’ was calculated for each of the 10,000 orientations using MTEX, followed by averaging to obtain \bar{M} . The incremental strain tensor used for calculation was

$$d\epsilon_{ij}^{sample} = d\epsilon_{xx} \begin{bmatrix} 1 & 0 & 0 \\ 0 & -\rho & 0 \\ 0 & 0 & 1-\rho \end{bmatrix}; \rho = -\frac{de_w}{de_l} \quad (20)$$

Here, de_w and de_l are the incremental strains along the width and

longitudinal direction. In general, textured sheets tend to deform with the minimum expenditure of energy [29]. Therefore, \bar{M} was evaluated for different values of ρ to identify the minima in the curve (Fig. 12b) and determine the relevant combination of \bar{M} and ρ for uniaxial tension along the X-axis (rolling direction). It can be observed that $\rho = 0.53$ corresponds to the lowest value of $\bar{M} = 3.01$.

Considering the strengthening contribution of grain boundaries ($\sigma_{gb} = kd^{-1/2}, d = 45 \pm 15 \mu m, k = 0.065 \text{ MPam}^{1/2}, \sigma_{gb} = 10 \text{ MPa}$) and the values of σ_{dis} , σ_{ppt} and σ_{sol} , q and n listed in Tables 2 and 3, the yield

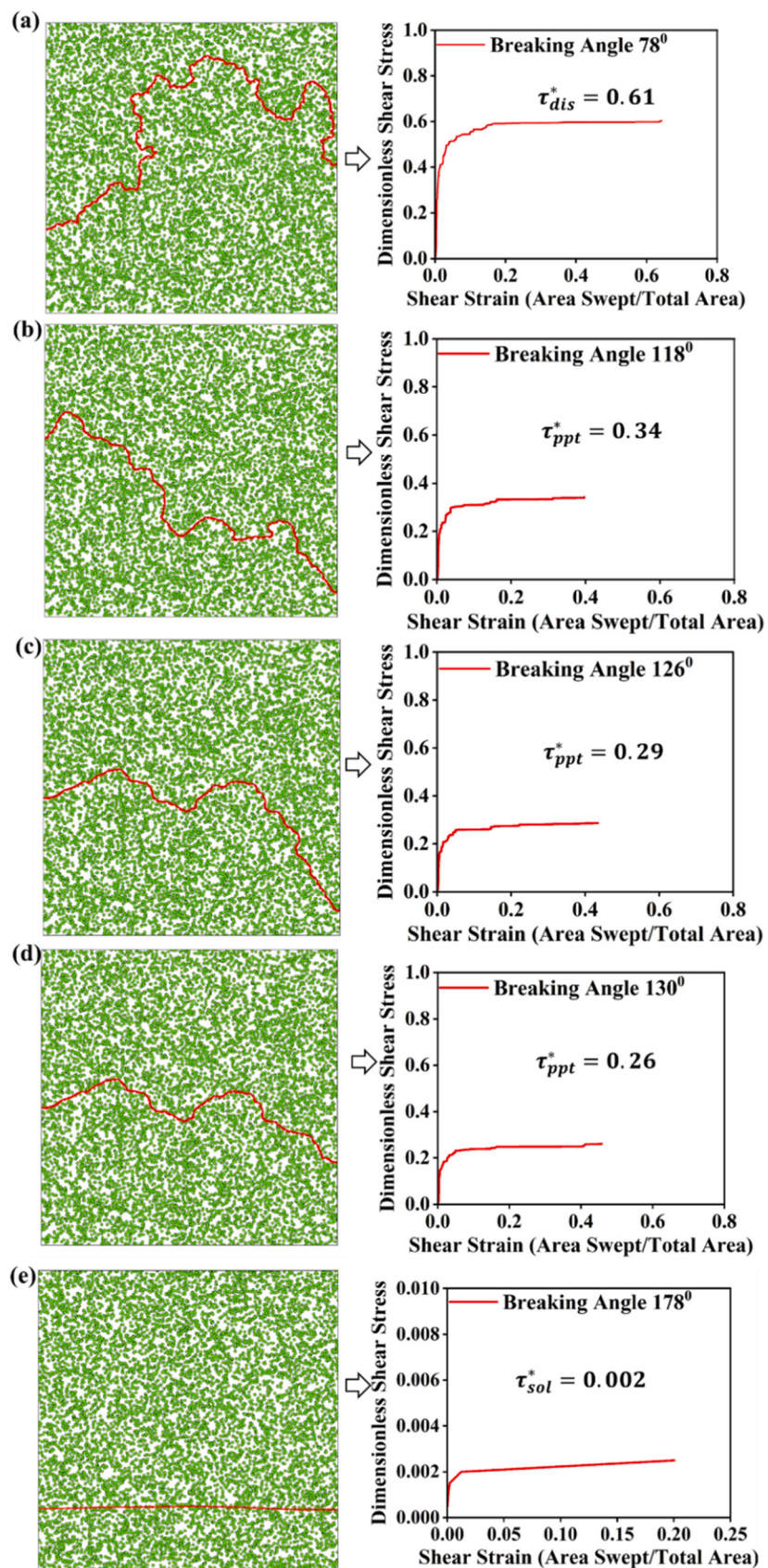


Fig. 11. The last stable dislocation configuration and the dimensionless shear stress versus shear strain curves for different breaking angles (a) 78° (b) 118° (c) 126° (d) 130° (e) 178° .

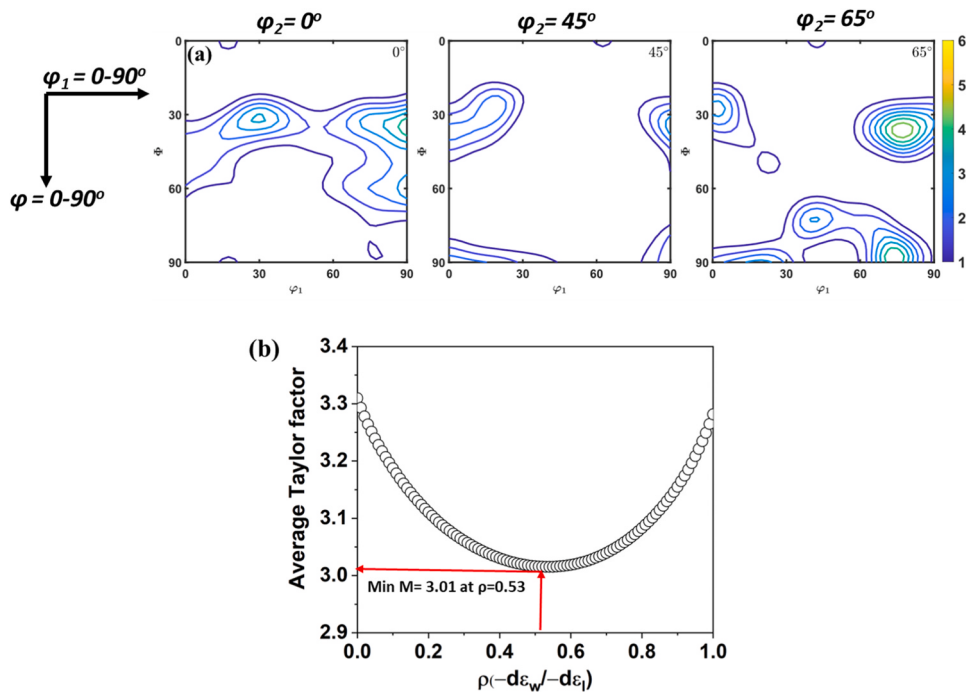


Fig. 12. (a) Important ODF sections ($\varphi_2 = 0^\circ$, 45° and 65°) representing the crystallographic texture of the solution treated sample (b) Evolution of average Taylor factor with the shape change factor ρ .

Table 3

Summary of dimensionless shear resistance of T_1 precipitates (τ_{ppt}^*), forest dislocations (τ_{dis}^*) and solutes (τ_{sol}^*), average Taylor factor, precipitate strengthening contribution (σ_{ppt}), forest dislocation strengthening contribution (σ_{dis}), solute strengthening contribution (σ_{sol}) and grain boundary strengthening contribution (σ_{gb}) for different pre-strained samples.

| Pre-strain | τ_{ppt}^* | τ_{dis}^* | τ_{sol}^* | \bar{M} | σ_{ppt} (MPa) | σ_{dis} (MPa) | σ_{sol} (MPa) | σ_{gb} (MPa) |
|------------|----------------|----------------|----------------|-----------|----------------------|----------------------|----------------------|---------------------|
| 5% | 0.34 | 0.61 | 0.002 | 3.01 | 218 | 283 | 44 | 10 |
| 10% | 0.29 | 0.61 | 0.002 | 3.01 | 198 | 355 | 44 | 10 |
| 20% | 0.24 | 0.61 | 0.002 | 3.01 | 171 | 432 | 44 | 10 |

strength was calculated using Eq. 6. It can be observed that the circle rolling method complemented by appropriate values of exponents q' and ' n ' results in an excellent agreement between the experimental and simulated values (Fig. 13a). In contrast, the previous approaches of using linear superposition [6,10] led to a significantly higher deviation between the experimental and simulated values (Fig. 13b). The advantage of using the circle rolling method to calculate the individual strengthening contributions over the traditional approach is illustrated in Fig. 13c. For T_1 precipitates, the following equation was proposed by Dorin et al. [6] to calculate σ_{ppt} .

$$\sigma_{ppt} = \frac{\bar{M} \times 1.211 \times D \times \gamma_{eff}^{3/2}}{t^2} \sqrt{\frac{bf_v}{T}} \quad (21)$$

Here, f_v is the volume fraction of the T_1 precipitates and T is the line tension ($Gb^2/2$). All the other terms are described previously in Eq. 12. Fig. 13c compares the σ_{ppt} values obtained from the circle rolling method (Eq. 17) and the above equation proposed by Dorin et al. [6]. It can be observed that Eq. 21 predicts a higher value of σ_{ppt} compared to the circle rolling method for a given pre-strain amount. Consequently, using Eq. 21 to calculate σ_{ppt} would have led to overestimation of the yield strength. By considering the statistical distribution of obstacles, there will always be some low resistance pathways on the glide plane through which dislocations can traverse relatively easily. Therefore, the circle rolling method predicts a lower value of σ_{ppt} compared to Eq. 21, which is based on the uniform distribution of precipitates on the glide plane.

6. Insights for developing high strength Al-Cu-Li alloys

Considering the yield strength of the 20% pre-strained sample (526 MPa) and the density of the AA 2195 alloy (~2.71 g/cc), the specific strength can be calculated as 194 kN m/kg, which is 70% of the specific strength of high strength steels (255 kN m/kg; yield strength \approx 2000 MPa; density \approx 7.86 g/cc). Therefore, Al-Cu-Li alloys have the potential to be equivalent to high strength steels in terms of specific strength if further improvement in yield strength can be achieved. As mentioned previously, T_1 precipitates are one of the major strengthening contributors in the Al-Cu-Li alloys. The traditional method of improving the strength of Al-Cu-Li alloys involves efforts to increase the number density of T_1 precipitates by applying pre-deformation prior to artificial ageing. In addition, it has been observed that precipitates with large aspect ratios (Diameter divided by thickness) cause further enhancement in the yield strength [30]. With the help of pre-deformation, the first objective of increasing the number density of the T_1 precipitates can be achieved (Table 1). However, the diameter of the T_1 precipitates decreased substantially with an increase in pre-strain from 5% to 20%. As a result, the strength of the T_1 precipitates (Eq. 12) decreased, which in turn hampered the strengthening increment. Hence, new protocols should be developed to increase the diameter of T_1 precipitates as the thickness remains more or less constant during low temperature ageing. The potential of 'aspect ratio hardening' for developing high strength Al alloys has not been fully explored. Fig. 14 summarizes the τ_{ppt}^* values for the 20% pre-strained sample and a few

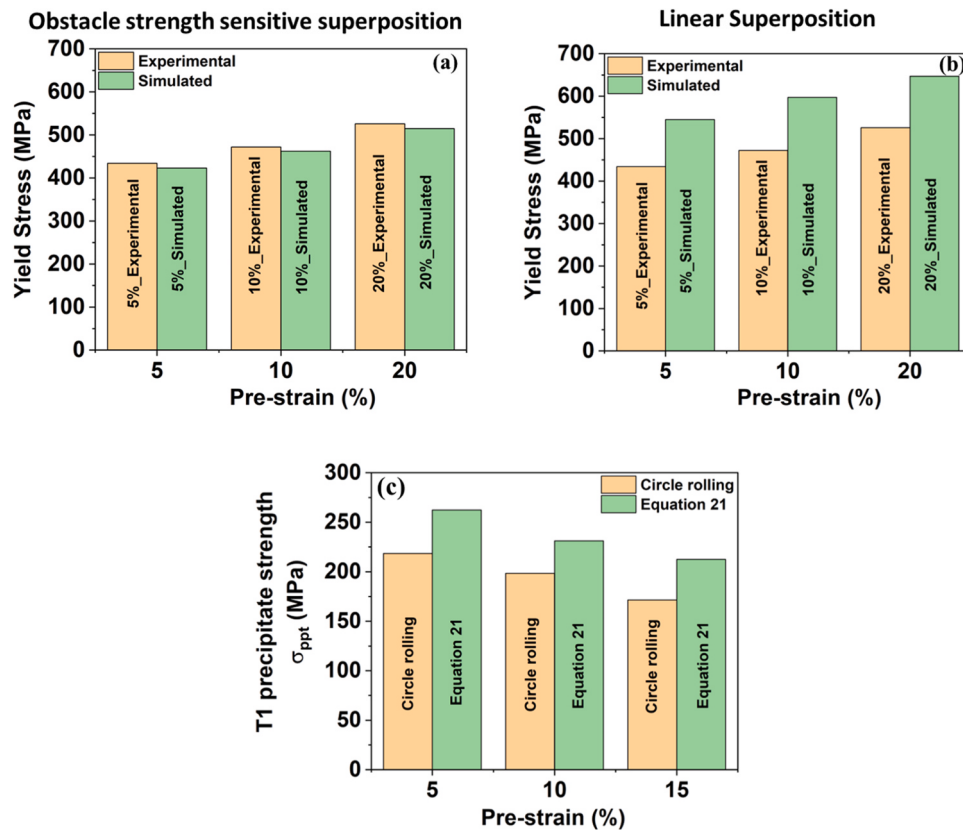


Fig. 13. Comparison between experimental and simulated yield strength values (a) Obstacle strength sensitive superposition (b) Linear superposition (c) Comparison between T_1 precipitate strength (σ_{ppt}) obtained from circle rolling method and Eq. 21.

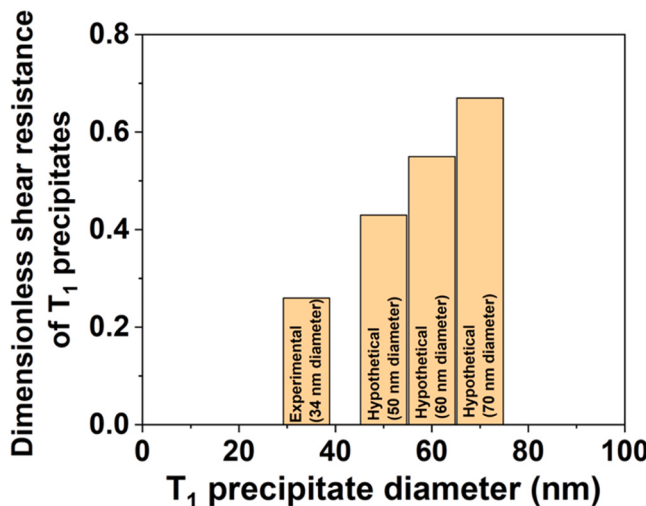


Fig. 14. Dimensionless shear resistance of T_1 precipitates for different diameters. Diameter of 34 nm corresponds to 20% pre-strained sample, while the others are hypothetical cases for comparison.

hypothetical data sets with progressively higher T_1 diameters. It can be observed that T_1 precipitates with a diameter of 70 nm have nearly three-times higher shear resistance compared to T_1 precipitates with a diameter of 34 nm. Therefore, novel alloy design methods and thermo-mechanical processing cycles should be developed to obtain T_1 precipitates with high aspect ratios. In the alloy design framework, the effect of microalloying elements on the aspect ratio of T_1 precipitates has been examined by a few authors [31–34]. It has been observed that Mg and Ag tend to augment the aspect ratio of the T_1 precipitates. The T_1

precipitate diameter increased from 42 nm in the ternary Al-Cu-Li alloy to 60 nm after the addition of 0.35 wt% Mg and 0.11 wt% Ag [31]. Therefore, further studies should be conducted to enhance the aspect ratio of T_1 precipitates by tailoring the microalloying content of Al-Cu-Li alloys. With respect to thermomechanical processing, no systematic studies have been conducted to establish a dislocation substructure that facilitates the formation of T_1 precipitates with high aspect ratios. The effect of the pre-straining temperature and mode on the dislocation density and patterning should be investigated to establish a favorable substructure for T_1 precipitates with high aspect ratios.

7. Summary

In the present work, circle rolling simulations and an obstacle strength sensitive flow stress superposition equation were used to understand the yield strength evolution of AA 2195 as a function of pre-strain. The key findings of this study are summarized below.

(i) The microstructure evolution during artificial ageing of AA 2195 is strongly dependent on the level of pre-strain. The number density of T_1 precipitates increased significantly with an increase in the pre-strain from 5% to 20%. On the other hand, the diameter of the T_1 precipitates decreased with increasing pre-strain.

(ii) Circle rolling simulations revealed that the dimensionless shear resistance of T_1 precipitates (τ_{ppt}^*) decreased at higher pre-strain levels owing to a reduction in the diameter of the T_1 precipitates (increase in the critical breaking angle).

(iii) The superposition exponent ‘ q ’ in the flow stress addition law increased with the pre-deformation because of the decrease in the difference between the critical breaking angles of the T_1 precipitates and solutes. However, the superposition exponent ‘ n ’ remains invariant to pre-strain, as it is dependent only on the critical breaking angles of the forest dislocations and solutes.

(iv) The yield strength prediction considering the dependence of the superposition exponent ‘*q*’ and ‘*n*’ on obstacle strength (critical breaking angles) provided the best agreement with the experimentally observed values. Linear superposition led to a gross overestimation of yield strength.

CRediT authorship contribution statement

Purnima Bharti: Investigation, Methodology, Data curation, Writing – original draft. **Ripudaman Singh:** Simulation, Formal analysis. **Jyoti Ranjan Sahoo:** Investigation, Data curation. **Aparna Tripathi:** Conceptualization, Formal analysis, Writing – review & editing. **Sumeet Mishra:** Conceptualization, Supervision, Writing – review & editing.

Declaration of Competing Interest

The authors declare that they have no known competing financial interests or personal relationships that could have appeared to influence the work reported in this paper.

Data Availability

Data will be made available on request. The raw/processed data required to reproduce these findings cannot be shared at this time as the data also forms part of an ongoing study.

Acknowledgements

Thanks are due to DST-SERB (SRG/2021/000346) for workstation facility. The authors would like to thank Dr. Manasij Yadava for important discussion on circle rolling algorithm.

Disclosure statement

No potential conflict of interest was reported by the authors.

References

- [1] J.-H. Kim, J.-H. Jeun, H.-J. Chun, Y.R. Lee, J.-T. Yoo, J.-H. Yoon, H.-S. Lee, Effect of precipitates on mechanical properties of AA2195, *J. Alloy. Compd.* 669 (2016) 187–198.
- [2] N. Nayan, S.V.S. Narayana Murty, A.K. Jha, B. Pant, S.C. Sharma, K.M. George, G. V.S. Sastry, Mechanical properties of aluminium–copper–lithium alloy AA2195 at cryogenic temperatures, *Mater. Des.* 58 (2014) 445–450.
- [3] W. Cassada, G. Shiflet, E. Starke, The effect of plastic deformation on Al₂CuLi (T 1) precipitation, *Metall. Trans. A* 22 (2) (1991) 299–306.
- [4] B. Gable, A. Zhu, A. Csontos, E. Starke, The role of plastic deformation on the competitive microstructural evolution and mechanical properties of a novel Al–Li–Cu–X alloy, *J. Light Met.* 1 (1) (2001) 1–14.
- [5] A. Zhu, E. Starke, Strengthening effect of unshearable particles of finite size: a computer experimental study, *Acta Mater.* 47 (11) (1999) 3263–3269.
- [6] T. Dorin, A. Deschamps, F.D. Geuser, C. Sigli, Quantification and modelling of the microstructure/strength relationship by tailoring the morphological parameters of the T1 phase in an Al–Cu–Li alloy, *Acta Mater.* 75 (Supplement C) (2014) 134–146.
- [7] A. Deschamps, B. Decreus, F. De Geuser, T. Dorin, M. Weyland, The influence of precipitation on plastic deformation of Al–Cu–Li alloys, *Acta Mater.* 61 (11) (2013) 4010–4021.
- [8] W. Poole, X. Wang, D. Lloyd, J. Embury, The shearable–non-shearable transition in Al–Mg–Si–Cu precipitation hardening alloys: implications on the distribution of slip, work hardening and fracture, *Philos. Mag.* 85 (26–27) (2005) 3113–3135.
- [9] J.F. Nie, B.C. Muddle, Microstructural design of high-strength aluminum alloys, *J. Phase Equilibria* 19 (6) (1998) 543–551.
- [10] B. Rodgers, P. Prangnell, Quantification of the influence of increased pre-stretching on microstructure-strength relationships in the Al–Cu–Li alloy AA2195, *Acta Mater.* 108 (2016) 55–67.
- [11] S. Ringer, B. Muddle, I. Polmear, Effects of cold work on precipitation in Al–Cu–Mg–(Ag) and Al–Cu–Li–(Mg–Ag) alloys, *Metall. Mater. Trans. A* 26 (7) (1995) 1659–1671.
- [12] N.Y. Zolotorevsky, A. Solonin, A.Y. Churumov, V. Zolotorevsky, Study of work hardening of quenched and naturally aged Al–Mg and Al–Cu alloys, *Mater. Sci. Eng.: A* 502 (1–2) (2009) 111–117.
- [13] Y. Huang, J. Robson, P. Prangnell, The formation of nanograin structures and accelerated room-temperature theta precipitation in a severely deformed Al–4 wt% Cu alloy, *Acta Mater.* 58 (5) (2010) 1643–1657.
- [14] V. Araullo-Peters, B. Gault, F. De Geuser, A. Deschamps, J.M. Cairney, Microstructural evolution during ageing of Al–Cu–Li–x alloys, *Acta Mater.* 66 (2014) 199–208.
- [15] A. de Vaucorbeil, W.J. Poole, C.W. Sinclair, The superposition of strengthening contributions in engineering alloys, *Mater. Sci. Eng.: A* 582 (2013) 147–154.
- [16] L. Cheng, W. Poole, J. Embury, D. Lloyd, The influence of precipitation on the work-hardening behavior of the aluminum alloys AA6111 and AA7030, *Metall. Mater. Trans. A* 34 (11) (2003) 2473–2481.
- [17] A. Foreman, M. Makin, Dislocation movement through random arrays of obstacles, *Philos. Mag.* 14 (131) (1966) 911–924.
- [18] T. Nogaret, D. Rodney, Finite-size effects in dislocation glide through random arrays of obstacles: Line tension simulations, *Phys. Rev. B* 74 (13) (2006), 134110.
- [19] U. Kocks, A statistical theory of flow stress and work-hardening, *Philos. Mag.* 13 (123) (1966) 541–566.
- [20] F. Bachmann, R. Hielscher, H. Schaeben, Texture analysis with MTEX-free and open source software toolbox, *Solid State Phenom., Trans. Tech. Publ.* (2010) 63–68.
- [21] G. Ribárik, B. Jóni, T. Ungár, The convolutional multiple whole profile (CMWP) fitting method, a global optimization procedure for microstructure determination, *Crystals* 10 (7) (2020) 623.
- [22] A. Kundu, D.P. Field, Influence of plastic deformation heterogeneity on development of geometrically necessary dislocation density in dual phase steel, *Mater. Sci. Eng.: A* 667 (2016) 435–443.
- [23] T. Abid, A. Boubertakh, S. Hamamda, Effect of pre-aging and maturing on the precipitation hardening of an Al–Mg–Si alloy, *J. Alloy. Compd.* 490 (1–2) (2010) 166–169.
- [24] T. Dorin, A. Deschamps, F. De Geuser, W. Lefebvre, C. Sigli, Quantitative description of the T1 formation kinetics in an Al–Cu–Li alloy using differential scanning calorimetry, small-angle X-ray scattering and transmission electron microscopy, *Philos. Mag.* 94 (10) (2014) 1012–1030.
- [25] B. Devincre, L. Kubin, Simulations of forest interactions and strain hardening in FCC crystals, *Model. Simul. Mater. Sci. Eng.* 2 (3A) (1994) 559.
- [26] B. Gault, F. de Geuser, L. Bourgeois, B.M. Gable, S.P. Ringer, B.C. Muddle, Atom probe tomography and transmission electron microscopy characterisation of precipitation in an Al–Cu–Li–Mg–Ag alloy, *Ultramicroscopy* 111 (6) (2011) 683–689.
- [27] A. Argon, 2007. Strengthening mechanisms in crystal plasticity, OUP Oxford 2007.
- [28] W.F. Hosford, The mechanics of crystals and textured polycrystals, 1993, Oxford University Press., USA, 1993, p. 248.
- [29] S. Mishra, M. Yadava, K. Kulkarni, N. Gurao, A modified Taylor model for predicting yield strength anisotropy in age hardenable aluminium alloys, *Mater. Sci. Eng.: A* 699 (2017) 217–228.
- [30] I. Polmear, D. St John, J.-F. Nie, M. Qian, Light alloys: metallurgy of the light metals, Butter -Heinemann (2017).
- [31] E. Gumbmann, F. De Geuser, C. Sigli, A. Deschamps, Influence of Mg, Ag and Zn minor solute additions on the precipitation kinetics and strengthening of an Al–Cu–Li alloy, *Acta Mater.* 133 (2017) 172–185.
- [32] E. Gumbmann, F. De Geuser, A. Deschamps, W. Lefebvre, F. Robaut, C. Sigli, A combinatorial approach for studying the effect of Mg concentration on precipitation in an Al–Cu–Li alloy, *Scr. Mater.* 110 (2016) 44–47.
- [33] D.L. Gilmore, E. Starke, Trace element effects on precipitation processes and mechanical properties in an Al–Cu–Li alloy, *Metall. Mater. Trans. A* 28 (7) (1997) 1399–1415.
- [34] B. Muddle, S. Ringer, I. Polmear, High strength microalloyed aluminium alloys, superconductors. Surfaces and Superlattices, Elsevier, 1994, pp. 999–1023.